WILEY-VCH

Advanced Electronic Materials, accepted Jan. 22, 2015
Article published online Feb. 14, 2015
DOI: 10.1002/aelm.201400022
Article type: Full Paper

Mechanism of Formation of the Thermoelectric Layered Cobaltate $Ca_3Co_4O_9$ by Annealing of CaO-CoO Thin Films

Biplab Paul[1,], Jeremy L. Schroeder[1], Sit Kerdsongpanya[1], Ngo Van Nong[2], Norbert Schell[3], Daniel Ostach[3], Jun Lu[1], Jens Birch[1], Per Eklund[1,*]*

[1]Thin Film Physics Division, Department of Physics, Chemistry, and Biology (IFM), Linköping University, SE-581 83 Linköping, Sweden

[2]Dept. of Energy Conversion and Storage, Technical University of Denmark, Risø Campus, Frederiksborgvej 399, Building 779, 4000 Roskilde, Denmark

[3]Helmholtz-Zentrum Geesthacht, Centre for Materials and Coastal Research, Institute for Materials Research, Max-Planck-Straße 1, 21502 Geesthacht, Germany

Keywords: Thermoelectrics, $Ca_3Co_4O_9$, thin film, sputtering, phase transformation

*Corresponding authors. E-mail bippa@ifm.liu.se; perek@ifm.liu.se

Abstract

The layered cobaltate $Ca_3Co_4O_9$ is of interest for energy-harvesting and heat-conversion applications because of its good thermoelectric properties and the fact that the raw materials Ca and Co are non-toxic, abundantly available, and inexpensive. While single-crystalline $Ca_3Co_4O_9$ exhibits high Seebeck coefficient and low resistivity, its widespread use is hampered by the fact that single crystals are too small and expensive. A promising alternative approach is the growth of highly textured and/or epitaxial $Ca_3Co_4O_9$ thin films with correspondingly anisotropic properties. Here, we present a two-step sputtering/annealing method for the formation of highly textured virtually phase-pure $Ca_3Co_4O_9$ thin films by reactive co-sputtering from Ca and Co targets followed by an annealing process at 730 °C under O_2-gas flow. The thermally induced phase transformation mechanism was investigated by *in-situ* time-resolved annealing experiments using synchrotron-based 2D x-ray diffraction as well as *ex-situ* annealing experiments and standard lab-based x-ray diffraction. By tuning the proportion of initial CaO and CoO phases during film deposition, the method enables synthesis of $Ca_3Co_4O_9$ thin films as well as Ca_xCoO_2. With this method, we demonstrate production of epitaxial $Ca_3Co_4O_9$ thin films with in-plane electrical resistivity of 6.44 mΩcm and a Seebeck coefficient of 118 μVK^{-1} at 300 K.

1. Introduction

Thermoelectrics have the potential to play an important role for thermal management and conversion of waste heat into electricity in environmentally friendly energy systems.[1, 2, 3] The power generation efficiency of a thermoelectric materials system is related to the dimensionless figure of merit $ZT=S^2T/\rho\kappa$, where S, T, ρ and κ are the Seebeck coefficient, absolute temperature, electrical resistivity, and thermal conductivity, respectively. High power generation efficiencies require high ZT values, which can be achieved with high-Seebeck materials that readily scatter phonons (low thermal conductivity) without impeding the transport of charge carriers (low electrical resistivity). Such an ideal thermoelectric material is often referred to as a 'phonon-glass-electron-crystal'.[4,5] Materials systems with layered structures are one approach towards realizing a 'phonon-glass-electron-crystal'. Alternating layers act as scattering layers for phonons and conducting layers for charge carriers. One class of layered thermoelectric materials are the misfit-layered cobalt oxides, which are described by the general formula $[M_mA_2O_{m+2}]_q[CoO_2]$ where M=Co, Bi, Pb, Tl, etc.; A=Ca, Sr, Ba, etc.; m=0, 1, 2, and $q \geq 0.5$.[6] The misfit-layered cobalt oxides are comprised of alternately stacked layers (along the c axis) of rocksalt-type $[M_mA_2O_{m+2}]$ layers, acting as phonon blocking layers, and CdI_2-type CoO_2 layers, acting as charge carrier conducting channels. This class of materials exhibits good thermoelectric properties, they are non-toxic, and the raw materials are abundant and inexpensive.[7]

The most important misfit-layered cobalt oxide is the archetype $Ca_3Co_4O_9$ (alternatively expressed as $[Ca_2CoO_3]_{0.62}[CoO_2]$), which exhibits a high Seebeck coefficient (S) and low electrical resistivity (ρ).[8, 9] The physical properties of $Ca_3Co_4O_9$ are anisotropic due to its inherently nanolaminated structure. Less resistive transport of charge carriers (e.g. 2 mΩcm at room temperature)[10] is practically realized in the basal plane of single crystalline

$Ca_3Co_4O_9$.[10,11] Despite these advantages, technical challenges and high cost associated with the growth of larger size $Ca_3Co_4O_9$ single crystals make them difficult to apply in practice. A more promising approach to exploit the anisotropic properties of $Ca_3Co_4O_9$ is the growth of textured and/or epitaxial $Ca_3Co_4O_9$ thin films, whose thermoelectric properties may be comparable to that of single crystalline $Ca_3Co_4O_9$. Synthesis of $Ca_3Co_4O_9$ thin films has been demonstrated by both chemical techniques and physical vapor deposition (PVD) techniques. Chemical synthesis methods include the chemical vapor deposition (CVD) techniques atomic layer deposition (ALD)[12] and metal-organic CVD,[13, 14] as well as chemical solution deposition methods followed by annealing,[15, 16, 17] and reactive solid-phase epitaxy by topotactic-ion exchange.[18, 19] However, PVD has broad advantages compared to chemical methods since PVD operates far from thermodynamic equilibrium and offers atomistic control of the deposition flux. PVD-based synthesis of $Ca_3Co_4O_9$ thin films has been demonstrated with both pulsed laser deposition[20, 21, 22, 23] and rf-magnetron sputtering[24, 25, 26] from compound targets of Ca-Co-O. However, sputter-deposition from compound targets suffers from two distinct drawbacks: 1) the Ca-Co-O ratio is fixed and the resultant film composition is often different from that of the target, and 2) deposition from an oxide target yields low deposition rates. Both of these drawbacks can be overcome by reactive co-sputtering from elemental targets (i.e. Ca and Co), thus making this approach more suitable for upscaling.

Here, we report a method for the growth of $Ca_3Co_4O_9$ thin films by a two-step sputtering/annealing method. CaO-CoO films are first deposited by reactive magnetron co-sputtering from Ca and Co targets followed by annealing in an oxygen atmosphere to form $Ca_3Co_4O_9$. The phase transformation mechanism is investigated by *in-situ* time-resolved annealing experiments using synchrotron-based x-ray diffraction (XRD) with a 2D-detector as well as *ex-situ* annealing experiments and standard lab-based XRD. The present method carries important advantages in that by tuning the proportion of initial CaO and CoO phases

during film deposition, the method enables synthesis of Ca_xCoO_2 thin films as well as $Ca_3Co_4O_9$. Further advantages include the high deposition rate (compared to deposition from oxide sources) associated with reactive sputter-deposition and the abundant availability of metallic Ca and Co targets. Thus, the present method offers prospects for upscaling and implementation in applications.

2. Results and discussion

2.1. As-deposited CaO-CoO and annealed Ca-Co-O films

The as-deposited CaO-CoO films are comprised of only CaO and CoO phases irrespective of the Ca:Co ratio in the films. Figure 1a shows a θ-2θ XRD scan for the as-deposited Ca:Co = 0.72 film. θ-2θ scans of as-deposited films with other Ca:Co elemental ratios were similar in appearance (not shown), albeit with varying CaO:CoO peak intensity ratios. The films were annealed at 730 °C for 4 hours under O_2 gas flow and the resultant phases were dependent on the initial Ca:Co ratio (Figure 1b – 1e). As expected, the annealed Ca:Co=0.72 film only shows the presence of $Ca_3Co_4O_9$ since its elemental ratio is closest to stoichiometric $Ca_3Co_4O_9$ (i.e. Ca:Co=0.75). As discussed below, a small amount of interfacial Ca_xCoO_2 (with overlapping peaks with $Ca_3Co_4O_9$) is also present. The $Ca_3Co_4O_9$ diffraction peaks occur for 001, 002, 003, 004, 006, and 008 $Ca_3Co_4O_9$. The 005 peak of $Ca_3Co_4O_9$ coincides with the large 006 peak of Al_2O_3. The Ca:Co=0.72 film exhibited an epitaxial relationship of $\{001\}Ca_3Co_4O_9 \| \{0001\}Al_2O_3$ and $\langle 010 \rangle Ca_3Co_4O_9 \| \langle \bar{2}110 \rangle Al_2O_3$, as verified by XRD pole figures (see Supplementary Information).

Films with other Ca:Co ratios show the presence of $Ca_3Co_4O_9$ in varying degrees in addition to other phases, depending on whether the initial film was Ca-rich or Co-rich. For

example, the Ca:Co=0.85 film is Ca-rich and shows the additional presence of CaO (Figure 1e) whereas the Ca:Co=0.69 is Co-rich and shows the additional presence of Co_3O_4 (Figure 1c). The Ca:Co=0.47 film is also Co-rich, but exhibits a Ca:Co elemental ratio within the stoichiometric window of Ca_xCoO_2, where x ranges between 0.26 and 0.5.[27] Therefore, the Ca:Co=0.47 film is constituted mainly of the Ca_xCoO_2 phase, which is manifested by strong diffraction peaks at 2θ = 16.425°, 33.275°, 49.275°, and 69.675° from the (001), (002), (003) and (004) planes of the Ca_xCoO_2 phase, respectively (Figure 1b). The additional low intensity diffraction peaks are attributed to the presence of minor concentrations of $Ca_3Co_4O_9$ and Co_3O_4 phases. The results from the annealed Ca:Co=0.47 and Ca:Co=0.72 films show that the present two-step sputtering/annealing method can be employed to grow two of the known ternary layered phases in the Ca-Co-O system (i.e. Ca_xCoO_2 and $Ca_3Co_4O_9$).

Identifying the Ca_xCoO_2 concentration from XRD patterns is difficult since all of the Ca_xCoO_2 peaks overlap with various $Ca_3Co_4O_9$ peaks. Therefore, we use a simplified approach for monitoring the progress of $Ca_3Co_4O_9$ formation. The peak at 2θ = 8.225° is solely originating from the (001) plane of $Ca_3Co_4O_9$, whereas the peak at 2θ = 16.425° is a convolution of the $Ca_3Co_4O_9$ 002 and Ca_xCoO_2 001 peaks. Defining I_1 as the integrated peak intensity of the 2θ = 8.225° peak and I_2 as the integrated peak intensity of the 2θ = 16.425° peak, the I_2/I_1 ratio provides a qualitative comparative measure of the $Ca_3Co_4O_9$ content, with lower I_2/I_1 values indicating higher $Ca_3Co_4O_9$ content. Figure 1 displays the I_2/I_1 values for each of the annealed films. Since the Ca:Co=0.72 film was verified by transmission electron microscopy (TEM, see next paragraph) to be nearly phase pure, the I_2/I_1 value for the Ca:Co=0.72 film is considered the baseline for phase purity. Any decrease from this baseline value indicates the partial presence of the Ca_xCoO_2 phase in the off-stoichiometric film.

Figure 2a shows a typical TEM image of an annealed Ca:Co=0.72 film. The high-resolution TEM (HRTEM) image in Figure 2b shows the layered structure of $Ca_3Co_4O_9$. The atomic arrangement of Ca, Co, and O atoms is schematically presented next to the HRTEM image. Compositional analyses and lattice imaging show that a region up to 17 nm from the substrate surface consists of the Ca_xCoO_2 phase. The presence of Ca_xCoO_2 near the interface is attributed to a Ca-deficiency near the substrate surface in the as-deposited films. This Ca-deficiency was observed in as-deposited films by energy dispersive x-ray spectroscopy (EDS) mapping of a TEM cross section (see Figure S2 in Supplementary Information). The Ca-deficiency occurs due to the segregation of thermally driven Ca near the surface of the as-deposited films, which is caused by substrate heating during sputter deposition. The *d* spacing of planes of $Ca_3Co_4O_9$ along the *c* direction is observed to be ~10.7 Å, which is consistent with the *d* spacing calculated from the *00l* peaks of the θ-2θ scan. The *d* spacing of the planes of Ca_xCoO_2 in the same direction is calculated to be ~5.41 Å, which is close to the reported value of 5.44 Å.[27]

2.2. *In-situ* time-resolved synchrotron-based x-ray diffraction study

A 260 nm CaO-CoO film with Ca:Co=0.72 was characterized by *in-situ* time-resolved synchrotron-based two-dimensional (2D) XRD during annealing in order to determine the details of the thermally induced phase transformation process from CaO-CoO films into $Ca_3Co_4O_9$. The film was annealed in a pure oxygen atmosphere with a continuous flow of pure oxygen (100 sccm). The annealing time/temperature profile is shown in Figure 3b. In brief, the film was ramped (8 K/min) to 720 °C, held at 720 °C for 135 minutes, ramped to 800 °C, held for 60 minutes, ramped to 880 °C, held for 10 minutes, ramped to 960 °C, held for 6 minutes, ramped to 1040 °C, held for 6 minutes, ramped to 1120 °C, and held for 5 minutes.

Figure 3a shows relevant sections of the 2D synchrotron-based XRD images during annealing, in which CaO, CoO, Co_3O_4, Ca_xCoO_2 and $Ca_3Co_4O_9$ are present at various stages of the annealing process (a time-resolved video is also available as Supporting Information). The diffraction images show that CoO first oxidizes to the intermediate Co_3O_4 phase, which then reacts with CaO to form Ca_xCoO_2. Ca_xCoO_2 subsequently reacts with CaO to form the $Ca_3Co_4O_9$ phase. As the 00*l* diffraction spots of Ca_xCoO_2 coincide with those of $Ca_3Co_4O_9$, they are indistinguishable in the 2D diffraction images. The formation of Ca_xCoO_2 as an intermediate phase via the reaction of Co_3O_4 with CaO was verified by *ex-situ* annealing and XRD experiments as described in the next section. It is apparent that those 2D diffraction spots will initially be from the (001) and (002) planes of Ca_xCoO_2 and at the end from the (002) and (004) planes of $Ca_3Co_4O_9$. Annealing temperatures above 880 °C led to the loss of calcium from $Ca_3Co_4O_9$ and the formation of CoO and Co_3O_4 cobalt oxide phases.

2D diffraction images were acquired every 13 seconds in order to follow the evolution of the transformation process. Figure 3b presents the evolution of the integrated peak intensity for the CaO, CoO, Co_3O_4, and Ca_xCoO_2/$Ca_3Co_4O_9$ reflections. Seven zones of interest are defined by dashed lines. At the onset (zone 1) only CaO and CoO phases are present in the films and their concentrations remain constant in the beginning stages of the annealing process. At ~ 620 °C, CoO starts to oxidize into Co_3O_4 (zone 2) as evidenced by the onset of a decline in the integrated peak intensity of CoO with a concomitant increase in the integrated peak intensity of Co_3O_4. After 3 minutes at 720 °C, the amount of CaO begins to decrease as it reacts with Co_3O_4 to form Ca_xCoO_2 and at the same time Ca_xCoO_2 is consumed by the reaction with CaO to form $Ca_3Co_4O_9$ (zone 3), whereby the integrated peak intensity for Ca_xCoO_2/$Ca_3Co_4O_9$ compounds begins to increase. Thus, there is competition between the formation and consumption of Ca_xCoO_2, with the formation rate expected to be higher in zone

3. A similar competition also occurs between the formation and consumption of Co_3O_4 whereby CoO transforms into Co_3O_4 while Co_3O_4 is simultaneously being consumed by the reaction with CaO to form Ca_xCoO_2. The consumption rate of Co_3O_4 is higher in zone 3 as evidenced by the downward trend of the Co_3O_4 integrated peak intensity. The onset of zone 4 is characterized by the CoO phase being exhausted, which results in the cessation of Co_3O_4 formation. The supply of Co_3O_4 is now limited, so the rate of Ca_xCoO_2/$Ca_3Co_4O_9$ formation decreases as evidenced by the decreasing slopes in the Ca_xCoO_2/$Ca_3Co_4O_9$ and CaO curves in zone 4. The Ca_xCoO_2 and $Ca_3Co_4O_9$ phases coexist in zone 4 and the complete phase transformation to $Ca_3Co_4O_9$ is not yet finished. Zone 5 starts when the temperature is increased to 800 °C. The increased temperature leads to increased reaction rates as shown by the changes in slope for all curves. In zone 5, the consumption rate of Ca_xCoO_2 by the reaction with CaO to form $Ca_3Co_4O_9$ becomes higher than its formation rate by the reaction of CaO and Co_3O_4 since the Co_3O_4 is gradually disappearing. In zone 6, the phase transformation to $Ca_3Co_4O_9$ comes to its end, which is evident from the decreasing slope of $Ca_3Co_4O_9$ integrated peak intensity. Further increases in temperature to 880 °C, 960 °C, 1040 °C, and 1120 °C (zone 7) lead to the evaporation of Ca from the lattice and the formation of CoO and Co_3O_4. Therefore, the $Ca_3Co_4O_9$ films are not stable at temperatures above 880 °C.

From the *in-situ* time-resolved synchrotron-based x-ray diffraction study it is concluded that the formation of Ca_xCoO_2 and $Ca_3Co_4O_9$ is initiated by the formation of Co_3O_4. Complete transformation to the final phase of $Ca_3Co_4O_9$ occurs in the temperature range 720 °C < T < 800 °C. Annealing at temperature at or above 880 °C leads to the decomposition of $Ca_3Co_4O_9$.

2.3. *Ex-situ* study of phase transformation

Ex-situ studies provide complementary information to the synchrotron-radiation studies. A CaO-CoO film with Ca:Co=0.72 was characterized by *ex-situ* annealing and XRD experiments in order to distinguish the Ca_xCoO_2 and $Ca_3Co_4O_9$ phases. The film was subjected to different annealing conditions in six sequential steps, as illustrated in Figure 4. Figure 5a shows the θ-2θ XRD scan for the as-deposited film while Figures 5b - 5g show θ-2θ scans after each annealing step.

After annealing step 1 (Figure 5b), the appearance of Co_3O_4 peaks with a concomitant decrease in the peak intensity of CoO indicates the reaction of CoO with oxygen to form Co_3O_4. The Co_3O_4 has also reacted with CaO to form the Ca_xCoO_2-phase as confirmed by the peaks at 2θ = 16.425°, 33.275°, and 69.675°, which are the Ca_xCoO_2 001, 002, and 004 peaks, respectively. These results indicate a competition between the formation and consumption of Co_3O_4.

After annealing step 2 (Figure 5c), the Ca_xCoO_2 phase becomes more intense, the CoO phase has disappeared, and the $Ca_3Co_4O_9$ phase has begun developing as evidenced by the $Ca_3Co_4O_9$ 001 and $Ca_3Co_4O_9$ 003 reflections (2θ = 8.225° and 2θ = 24.925°, respectively). It should be noted that the *d* spacing of the *c* planes in Ca_xCoO_2 (~5.41 Å) is almost half of the *c* lattice parameter of $Ca_3Co_4O_9$ (~10.8 Å), resulting in the near-coincidence of some of the $Ca_3Co_4O_9$ 00*l* peaks with the Ca_xCoO_2 00*l* peaks, thus making it difficult to distinguish these two phases. However, the $Ca_3Co_4O_9$ 001 (2θ =8.225°) and $Ca_3Co_4O_9$ 003 (2θ =24.925°) peaks do not overlap with any Ca_xCoO_2 peaks.

The I_2/I_1 integrated peak intensity ratio in Figure 5c is much larger than the I_2/I_1 ratio for the $Ca_3Co_4O_9$ film in Figure 1c, indicating that Ca_xCoO_2 is the dominant phase. The Ca_xCoO_2 and $Ca_3Co_4O_9$ phases exhibit overlapping peaks at 2θ angles of 16.425°, 33.275°, 51.025°, and 69.675°. The $Ca_3Co_4O_9$ phase appears at slightly larger 2θ values than the Ca_xCoO_2 phase. Therefore, small shifting of the overlapping peaks towards higher 2θ values with increased annealing time provides further evidence of the phase transformation from Ca_xCoO_2 to $Ca_3Co_4O_9$. Figure 6 shows enlarged θ-2θ scans for the peaks labeled as I_1 and I_2. The I_1 peak is the $Ca_3Co_4O_9$ 001 reflection and increased annealing time leads to increased intensity, but no peak shift. On the other hand, the I_2 peak is a convolution of the Ca_xCoO_2 001 and $Ca_3Co_4O_9$ 002 reflections, which have slightly different d spacings. Therefore, increased annealing time leads to increased $Ca_3Co_4O_9$ intensity, decreased Ca_xCoO_2 intensity, and an associated shift in the I_2 peak towards higher 2θ values. From these results, we conclude that three different phase transformation processes (i.e., CoO + O2 $\Rightarrow$ Co_3O_4; Co_3O_4 + CaO $\Rightarrow$ Ca_xCoO_2; and Ca_xCoO_2 + CaO $\Rightarrow$ $Ca_3Co_4O_9$) are simultaneously occurring at temperatures above 520 °C and the reaction process can be monitored through the I_2/I_1 ratio.

After annealing step 3 (Figure 5d), the $Ca_3Co_4O_9$ phase becomes more intense, the Co_3O_4 phase has disappeared, and the CaO phase intensity begins decreasing. The phase transformation process continues to proceed with increased annealing time (step 4, Figure 5e), but the presence of CaO peaks indicates that the phase transformation process is not yet completed. Further annealing at higher temperature (step 5, Figure 5f) shows complete consumption of CaO and a further decrease of the I_2/I_1 ratio. The only peaks remaining are associated with the $Ca_3Co_4O_9$-phase, indicating completion of the phase transformation.

Finally, annealing at 800 °C (step 6, Figure 5g) results in decomposition of $Ca_3Co_4O_9$ into Co_3Co_4 and CaO.

Ex-situ annealing and XRD experiments thus confirm that the transformation of CaO-CoO films into a layered $Ca_3Co_4O_9$ structure occurs via the intermediate formation of a layered Ca_xCoO_2 structure. $Ca_3Co_4O_9$ is the most stable phase in the temperature range of 700 – 775 °C for a Ca:Co elemental ratio of 0.72. In contrast, the Ca_xCoO_2 phase is stable from 500 °C to 775 °C for lower Ca content (cf., Figure 1).

2.4. Thermoelectric properties

Figures 7a, 7b, and 7c show the electrical resistivity, Seebeck coefficient, and power factor, respectively, as a function of temperature for samples with different Ca:Co ratio. The electrical resistivity (Figure 7a) of the Ca:Co=0.72 film is lower than that of the Ca-rich and Co-rich samples throughout the measured temperature range, owing to its phase purity. The room temperature electrical resistivity of the phase pure sample (6.44 mΩcm) is comparable to most $Ca_3Co_4O_9$ thin films grown by different techniques,[8-21] but somewhat higher than the lowest reported electrical resistivity value for $Ca_3Co_4O_9$ thin films deposited on glass substrates (~4 mΩcm).[28] The electrical resistivity of the Ca-rich and Co-rich samples increases with increasing deviation of the Ca:Co ratio from the stoichiometric limit, which is attributed to enhanced scattering of charge carriers by the grains of impurity oxide phases. The electrical resistivity of the $Ca_3Co_4O_9$ thin films is temperature independent up to about 275 °C followed by a systematic increase with increasing temperature. The increasing electrical resistivity beyond 275 °C is attributed to the release of oxygen from the films at high temperature. This is a known effect for $Ca_3Co_4O_9$ thin films when the measurements are performed in a low-pressure helium atmosphere and not in regular atmosphere.[29, 30,31] The

room-temperature electrical resistivity of Ca_xCoO_2 film with Ca:Co=0.47 is 208 mΩcm, which is higher than the reported value of 5 mΩcm for epitaxial phase-pure films,[32] as well as the value of 60.8 mΩcm for bulk polycrystalline Ca_xCoO_2 (x ~ 0.47),[33] The presence of $Ca_3Co_4O_9$ and Co_3O_4 phases in Ca_xCoO_2 (x ~ 0.47) film, as confirmed by XRD, explains the relatively high in-plane resistivity of the Ca_xCoO_2 film, which is attributed to the scattering of charge carriers at Ca_xCoO_2/ $Ca_3Co_4O_9$ and Ca_xCoO_2/Co_3O_4 interfaces in the film.

The Seebeck coefficient (Figure 7b) follows the same trends as electrical resistivity. The room temperature Seebeck coefficient of the Ca_xCoO_2 (x ~ 0.47) film is 135 μVK^{-1}, which is higher than the reported value of in-plane Seebeck coefficient 60 μVK^{-1} for Ca_xCoO_2 epitaxial thin films[32] and comparable to the value of 145 μVK^{-1} for bulk polycrystalline Ca_xCoO_2 (x ~ 0.47).[33] The room temperature Seebeck coefficient of the phase pure Ca:Co=0.72 film is 118 μVK^{-1}, which is consistent with reported values for $Ca_3Co_4O_9$ thin films.[34, 35] The power factor (Figure 7c) of the phase pure Ca:Co=0.72 film is substantially higher (above 2×10^{-4} $Wm^{-1}K^{-2}$ throughout the measured temperature range) than the other samples due to its lower electrical resistivity. The maximum power factor is 3×10^{-4} $Wm^{-1}K^{-2}$ at about 350 °C for the phase pure Ca:Co=0.72 film. Figure 7d shows the integrated peak intensity ratio I_2:I_1 and the room temperature power factor as a function of the Ca:Co elemental ratio. The power factor is highest for the Ca:Co = 0.72 film and falls when the Ca:Co ratio deviates from near-stoichiometry.

3. Conclusion

We have demonstrated a two-step sputtering/annealing method for the formation of highly textured $Ca_3Co_4O_9$ thin films from reactively co-sputtered CaO-CoO thin films. The same method was also demonstrated to enable the growth of Ca_xCoO_2 thin films. With this method,

individual compositional control is possible by tuning the Ca/Co ratio. The *in-situ* time-resolved annealing experiments using synchrotron-based XRD as well as *ex-situ* annealing experiments revealed that the thermally induced phase transformation into $Ca_3Co_4O_9$ consists of the following steps:

1. $CoO + O_2 \Rightarrow Co_3O_4$
2. $Co_3O_4 + CaO \Rightarrow Ca_xCoO_2$
3. $Ca_xCoO_2 + CaO \Rightarrow Ca_3Co_4O_9$.

Highly textured $Ca_3Co_4O_9$ thin films exhibit good thermoelectric properties, which may be further improved by ensuring uniform distribution of CaO and CoO phases in the as-deposited film, e.g., by sequential deposition. Apart from the high degree of control over phase composition and chemical composition, the abundant availability of the metallic Ca and Co targets and the high rate deposition rate of reactive sputtering imply the suitability for industrial upscaling and implementation in applications.

4. Experimental section

$Ca_3Co_4O_9$ thin films were prepared by a two-step deposition and annealing process. Prior to deposition, Al_2O_3(001) substrates were held at 700 °C for one hour. Then, CaO-CoO films were reactively co-sputtered from Ca and Co targets onto the Al_2O_3(001) substrates by rf-magnetron sputtering at 0.27 Pa (2 mTorr) in an oxygen (1.5 %) - argon (98.5 %) mixture. The deposition system is described elsewhere.[36, 37] Five series of samples with varying Ca:Co elemental ratio were deposited (Ca:Co=0.85, 0.81, 0.72, 0.69, 0.47) and a second series of Ca:Co=0.72 films was deposited to ensure process reproducibility. The structural properties of these Ca:Co=0.72 films were essentially the same and the Ca:Co elemental ratio corresponds to stoichiometric $Ca_3Co_4O_9$ within the error of the composition analysis. The

composition of the films was determined at different regions of the film surface by EDS, with an accuracy of ±5 %. The samples with Ca:Co=0.85 and 0.81 are Ca-rich, samples with Ca:Co = 0.72 are near-stoichiometric, and samples with Ca:Co=0.69 and 0.47 are Co-rich. The crystal structure and morphology of the films were characterized by θ-2θ x-ray diffraction and pole figure analyses using monochromatic Cu Kα radiation (λ=1.5406 Å), transmission electron microscopy (TEM), and scanning electron microscopy (SEM). The θ-2θ x-ray diffraction scans were performed with a Philips PW 1820 diffractometer while the pole figures were performed with a Philips X'pert materials research diffractometer operated with a point focus, primary optics of 2×2 mm^2 cross slits, and secondary optics with parallel-plate collimator.

In-situ annealing experiments using time-resolved synchrotron-based 2D x-ray diffraction were performed at the High Energy Materials Science Beamline (P07) at PETRA III, DESY, Hamburg, with 53.7 keV monochromatic x-rays and a slit-determined spot size of 0.5 mm x 2 mm. The 2D detector used was a Perkin Elmer 1621 Flat Panel, with 200 x 200 μm^2 pixel size and 2048 x 2048 array field of view.[38]

Ex-situ annealing and XRD experiments were performed on a single CaO-CoO thin film with Ca:Co = 0.72. The Ca:Co = 0.72 film was subjected to six sequential annealing steps and θ-2θ XRD scans were performed after each annealing step. The annealing furnace was stabilized at a given set-point temperature prior to inserting the sample for a specified time period. The sample temperature was monitored as a function of time via a thermocouple in contact with the film substrate. The sample was removed from the furnace after the specified annealing time and cooled in ambient air at room temperature, as illustrated in Figure 4. In steps 1 – 4, the furnace temperature was set at 710 °C and the sample was

annealed for 3, 5, 6 and 40 minutes corresponding to final sample temperatures of 520 °C, 640 °C, 680 °C, and 700 °C, respectively. In step 5, the furnace temperature was set at 790 °C and the sample was annealed for 29 minutes corresponding to a temperature of 775 °C. Finally, in step 6 the furnace temperature was set at 850 °C and the sample was annealed for 10 minutes corresponding to a temperature of 800 °C.

The temperature dependent in-plane electrical resistivity and Seebeck coefficient were simultaneously characterized using an ULVAC-RIKO ZEM3 system in a low-pressure helium atmosphere.

Supporting Information

Supporting Information is available from the Wiley Online Library or from the author.

Acknowledgements

The research leading to these results has received funding from the European Research Council under the European Community's Seventh Framework Programme (FP/2007-2013) / ERC grant agreement no 335383, the Swedish Research Council (VR) under project no 2012-4430, the RÅC Frame Program (2011-6505) and the Linnaeus Strong Research Environment LiLi-NFM, and the Swedish Foundation for Strategic Research (SSF) through the Future Research Leaders 5 program. N. V. N. acknowledges the support by the NAFOSTED grant under proposal 103.02-2013.52.

References

[1] L. L. Baranowski, G. J. Snyder, E. S. Toberer, *Energy Environ. Sci.* **2012**, *5*, 9055.
[2] S. B. Viklund, M. T. Johansson, *Energy Convers. Manage.* **2014**, *77*, 369.
[3] A. Date, A. Date, C. Dixon, A. Akbarzadeh, *Ren. Sus. Energy Rev.* **2014**, *33*, 371.
[4] G. J. Snyder, E. S. Toberer, *Nat. Mater.* **2008**, *7*, 105.
[5] G. J. Snyder, M. Christensen, E. Nishibori, T. Caillat, B. B. Iversen, *Nat. Mater.* **2004**, *3*, 458.
[6] H. Yamauchi, L. Karvonen, T. Egashira, Y. Tanaka, M. Karppinen, *J. Solid State Chem.* **2014**, *184*, 64.
[7] M. W. Gaultois, T. D. Sparks, C. K. H. Borg, R. Seshadri, W. D. Bonificio, D. R. Clarke, *Chem. Mater.* **2013**, *25*, 2911.
[8] J. Yang, H.–L. Yip, A. K.–Y. Jen, *Adv. Energy Mater.* **2013**, *3*, 549.
[9] N. V. Nong, N. Pryds, S. Linderoth, M. Ohtaki, *Adv. Mater.* **2011**, *23*, 2484.
[10] M. Shikanoa, R. Funahashi, *Appl. Phys. Lett.* **2003**, *82*, 1851.
[11] R. Funahashi, I. Matsubara, H. Ikuta, T. Takeuchi, U. Mizutani, S. Sodeoka, *Jpn. J. Appl. Phys.* **2000**, *39*, L1127.
[12] J. Lybeck, M. Valkeapaa, S. Shibasaki, I. Terasaki, H. Yamauchi, M. Karppinen, *Chem. Mater.* **2010**, *22*, 5900.
[13] S. Wang, M. Chem, L. He, J. Zheng, W. Yu, G. Fu, *J. Phys. D: Appl. Phys.* **2009**, *42*, 045410.
[14] I. Matsubara, R. Funahashi, M. Shikano, K. Sasaki, H. Enomoto, *Appl. Phys. Lett.* **2002**, *80*, 4729.
[15] X. Zhu, D. Shi, A. Dou, Y. Sun, Q. Li, L. Wang, W. Li, W. Yeoh, R. Zheng, Z. Chen, C. Kong, *Acta Materialia* **2010**, *58*, 4281.
[16] R. Wei, H. Jian, X. Tang, J. Yang, L. Hu, L. Chen, J. Dai, X. Zhu, Y. Sun, *J. Am. Ceram. Soc.* **2013**, *96*, 2396.
[17] C.-J. Liu, P. K. Nayak, Z.-R. Li, K.-Y. Jeng, *Thin Solid Films* **2008**, *516*, 8564.
[18] K. Sugiura, H. Ohta, K. Koumoto, *Int. J. Appl. Ceram. Technol.* **2007**, *4*, 308.
[19] K. Sugiura, H. Ohta, K. Nomura, T. Satio, Y. Ikuhara, M. Hirano, H. Hosono, K. Koumoto, *Mater. Trans.* **2007**, *48*, 2104.
[20] Y. F. Hu, W. D. Si, E. Sutter, Q. Li, *Appl. Phys. Lett.* **2005**, *86*, 082103.
[21] H. Minami, K. Itaka, H. Kawaji, Q. J. Wang, H. Koinuma, M. Lippmaa, *Appl. Surf. Sci.* **2002**, *197*, 442.
[22] H. P. An, C. H. Zhu, W. W. Ge, Z. Z. Li, G. D. Tang, *Thin Solid Films* **2013**, *545*, 229.
[23] T. Sun, H. H. Hng, Q. Y. Yan, J. Ma, J. Appl. Phys. **2010**, *108*, 083709.
[24] A. Sakai, T. Kanno, S. Yotsuhashi, A. Odagawa, H. Adachi, *Jpn. J. Appl. Phys.* **2005**, *44*, L966.
[25] T. Kanno, S. Yotsuhashi, H. Adachi, *Appl. Phys. Lett.* **2004** , *85*, 739.
[26] M.-G. Kang, K.-H. Cho, S.-M. Oh, J.-S. Kim, C.-Y. Kang, S. Nahm, S.-J. Yoon, *Appl. Phys. Lett.* **2011**, *98*, 142102.
[27] B. L. Cushing, J. B. Wiley, *J. Solid State Chem.* **1998**, *141*, 385.
[28] Y. F. Hu, E. Sutter, W. D. Si, Q. Li, *Appl. Phys. Lett.* **2005**, *87*, 171912.
[29] Q. Qiao, A. Gulec, T. Paulauskas, S. Kolesnik, B. Dabrowski, M. Ozdemir, C. Boyraz, D. Mazumdar, A. Gupta, R. F. Klie, *J. Phys. Condens. Matter. B* **2011**, *23*, 305005.
[30] M. Schrade, H. Fjeld, T. G. Finstad, T. Norby, *J. Phys. Chem. C* **2014**, *118*, 2908.
[31] N. Van Nong, S. A. Junio, N. Pryds, S. Linderoth, *J. Elec. Mater.* **2012,** *41*, 1280.
[32] T. Kanno, S. Yotsuhashi, H. Adachi, *Appl. Phys. Lett.* **2004**, *85*, 739.
[33] Y. Miyazaki, X. Huang, T. Kajiwara, H. Yamane, T. Kajitani, *J. Ceram. Soc. Japan* **2009**, *117*, 42.

[34] T. Sun, J. Ma, Q. Y. Yan, Y. Z. Huang, J. L. Wang, H. H. Hng, *J. Cryst. Growth*, **2009**, *311*, 4123.
[35] Y. Fu, X. Tang, J. Yang, H. Jian, X. Zhu, Y. Sun, *J. Mater. Sci. Technol.* **2013**, *29*, 13.
[36] D. H. Trinh, M. Ottosson, M. Collin, I. Reineck, L. Hultman, H. Högberg, *Thin Solid Films* **2008,** *516*, 4977.
[37] J. Frodelius, P. Eklund, M. Beckers, P. O. Å. Persson, H. Högberg, L. Hultman, *Thin Solid Films* **2010**, *518*, 1621.
[38] N. Schell, A, King, F., Beckmann, T., Fischer, M., Müller, A. Schreyer, *Mat. Sci. Forum* **2014**, *772*, 57.

FIGURE CAPTIONS

Figure 1. θ-2θ x-ray diffraction patterns of a) as-deposited CaO-CoO film, and annealed films with b) Ca:Co=0.47, c) Ca:Co=0.69, d) Ca:Co=0.72, e) Ca:Co=0.85.

Figure 2. a) TEM image of Ca:Co=0.72 thin film showing the layered $Ca_3Co_4O_9$ structure with a 17 nm region from the interface comprised of Ca_xCoO_2. b) Lattice-resolved TEM image and schematic of the atomic arrangement of the layers.

Figure 3. a) 2D x-ray diffraction-based images for seven different zones of *in-situ* annealing experiments using time-resolved synchrotron-based 2D x-ray diffraction b) Integrated XRD peak intensities of different phases as a function of annealing time and temperature.

Figure 4. Time/temperature data for each *ex-situ* annealing step.

Figure 5. θ-2θ x-ray diffraction patterns of the Ca:Co=0.72 thin film as a function of annealing time and temperature.

Figure 6. θ-2θ x-ray diffraction patterns versus annealing temperature of a) the 001 $Ca_3Co_4O_9$ peak and b) the convoluted Ca_xCoO_2 001 and $Ca_3Co_4O_9$ 002 peaks. The peak shift in (b) with increasing temperature is related to the reaction $Ca_xCoO_2 + CaO = Ca_3Co_4O_9$.

Figure 7. Temperature dependent a) electrical resistivity, b) Seebeck coefficient, and c) power factor for all samples as a function of elemental ratio Ca:Co. d) I_2/I_1 ratio and room temperature value of power factor as a function of elemental ratio Ca:Co.

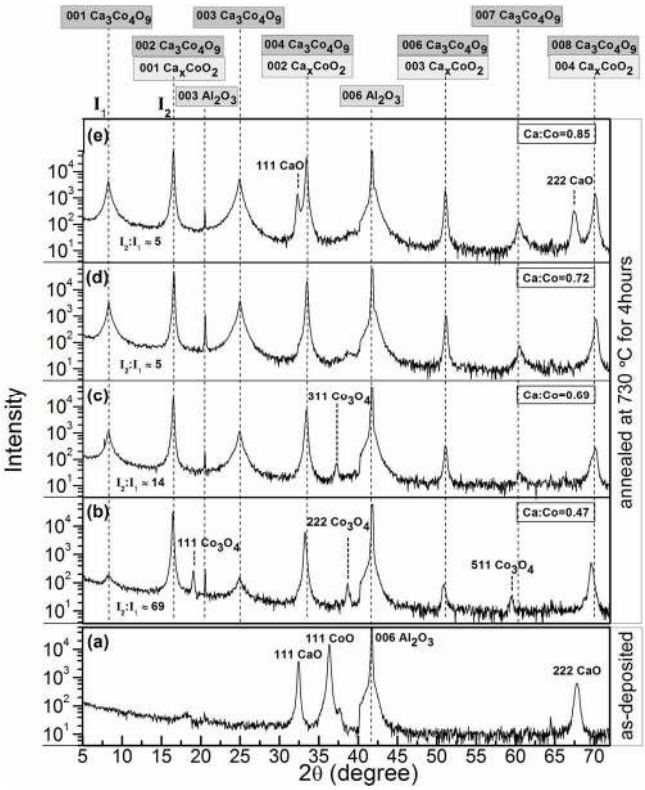

Figure 1. θ-2θ x-ray diffraction patterns of a) as-deposited CaO-CoO film, and annealed films with b) Ca:Co=0.47, c) Ca:Co=0.69, d) Ca:Co=0.72, e) Ca:Co=0.85.

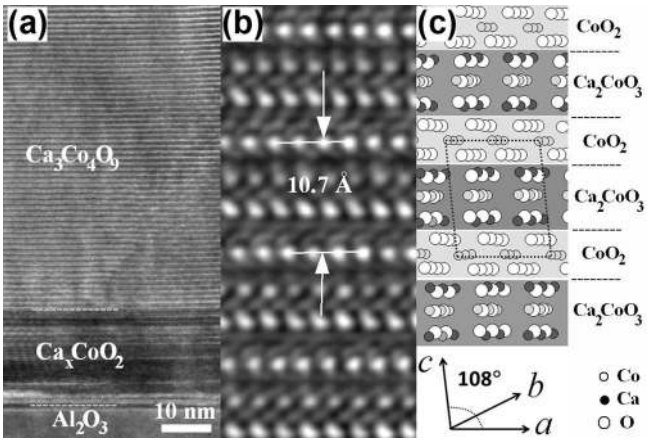

Figure 2. a) TEM image of Ca:Co=0.72 thin film showing the layered $Ca_3Co_4O_9$ structure with a 7 nm region from the interface comprised of Ca_xCoO_2. b) Lattice-resolved TEM image and schematic of the atomic arrangement of the layers.

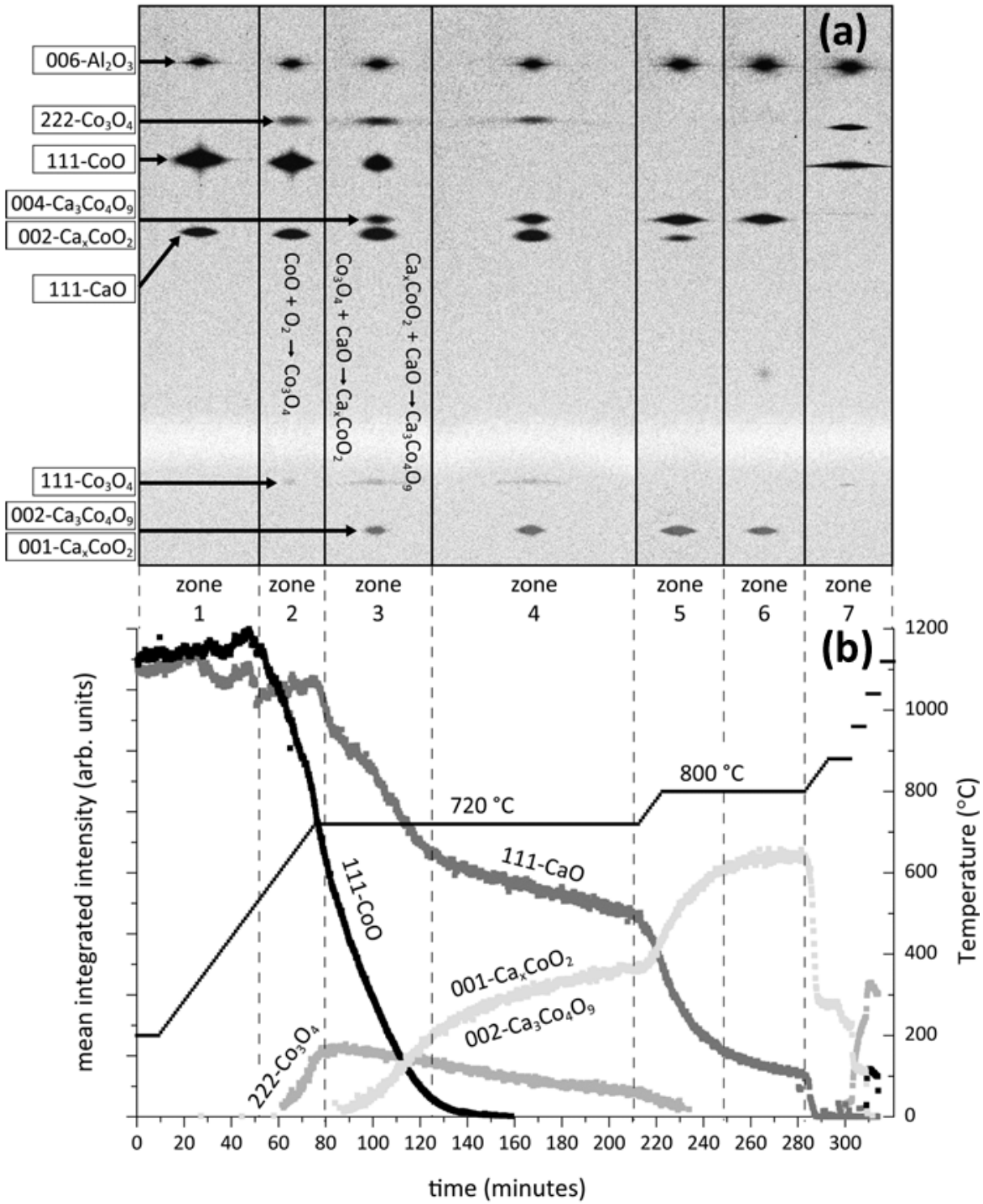

Figure 3. a) 2D x-ray diffraction-based images for seven different zones of *in-situ* annealing experiments using time-resolved synchrotron-based 2D x-ray diffraction b) Integrated XRD peak intensities of different phases as a function of annealing time and temperature.

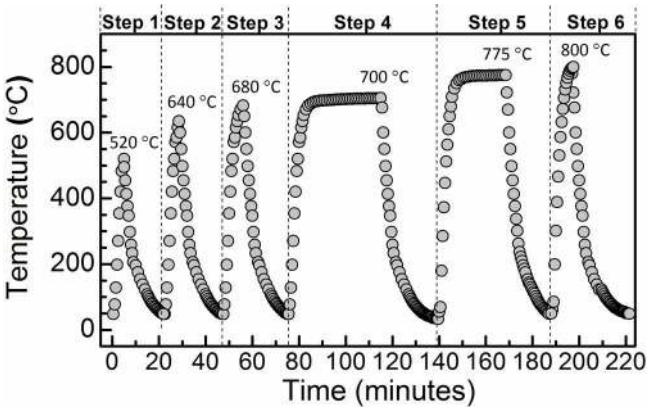

Figure 4. Time/temperature data for each *ex-situ* annealing step.

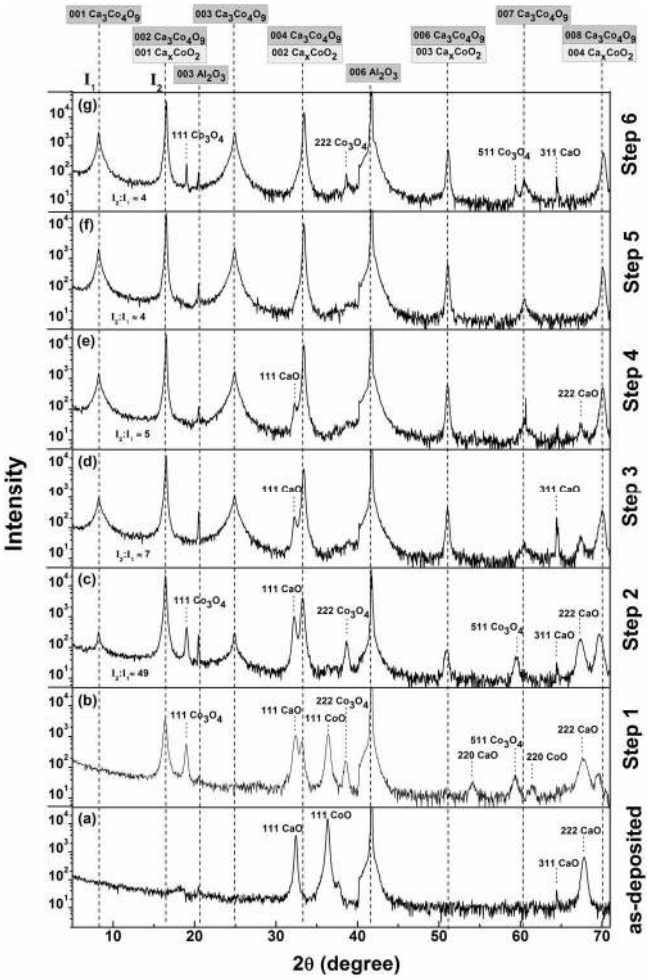

Figure 5. θ-2θ x-ray diffraction patterns of the Ca:Co=0.72 thin film as a function of annealing time and temperature.

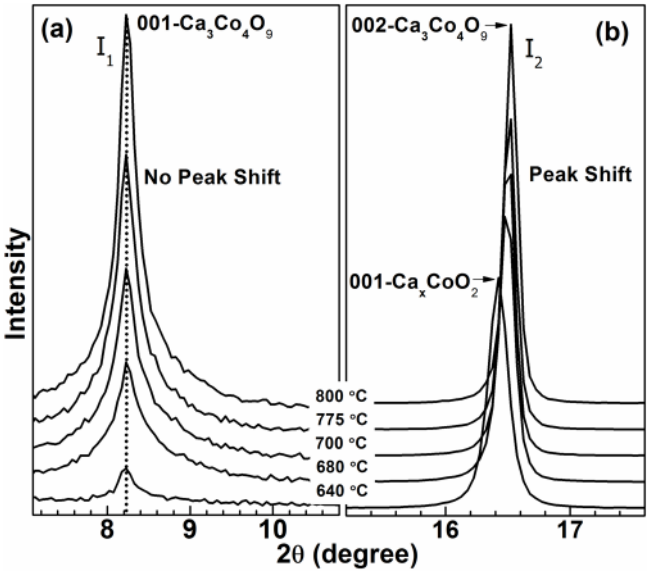

Figure 6. θ-2θ x-ray diffraction patterns versus annealing temperature of a) the 001 $Ca_3Co_4O_9$ peak and b) the convoluted Ca_xCoO_2 001 and $Ca_3Co_4O_9$ 002 peaks. The peak shift in (b) with increasing temperature is related to the reaction $Ca_xCoO_2 + CaO = Ca_3Co_4O_9$.

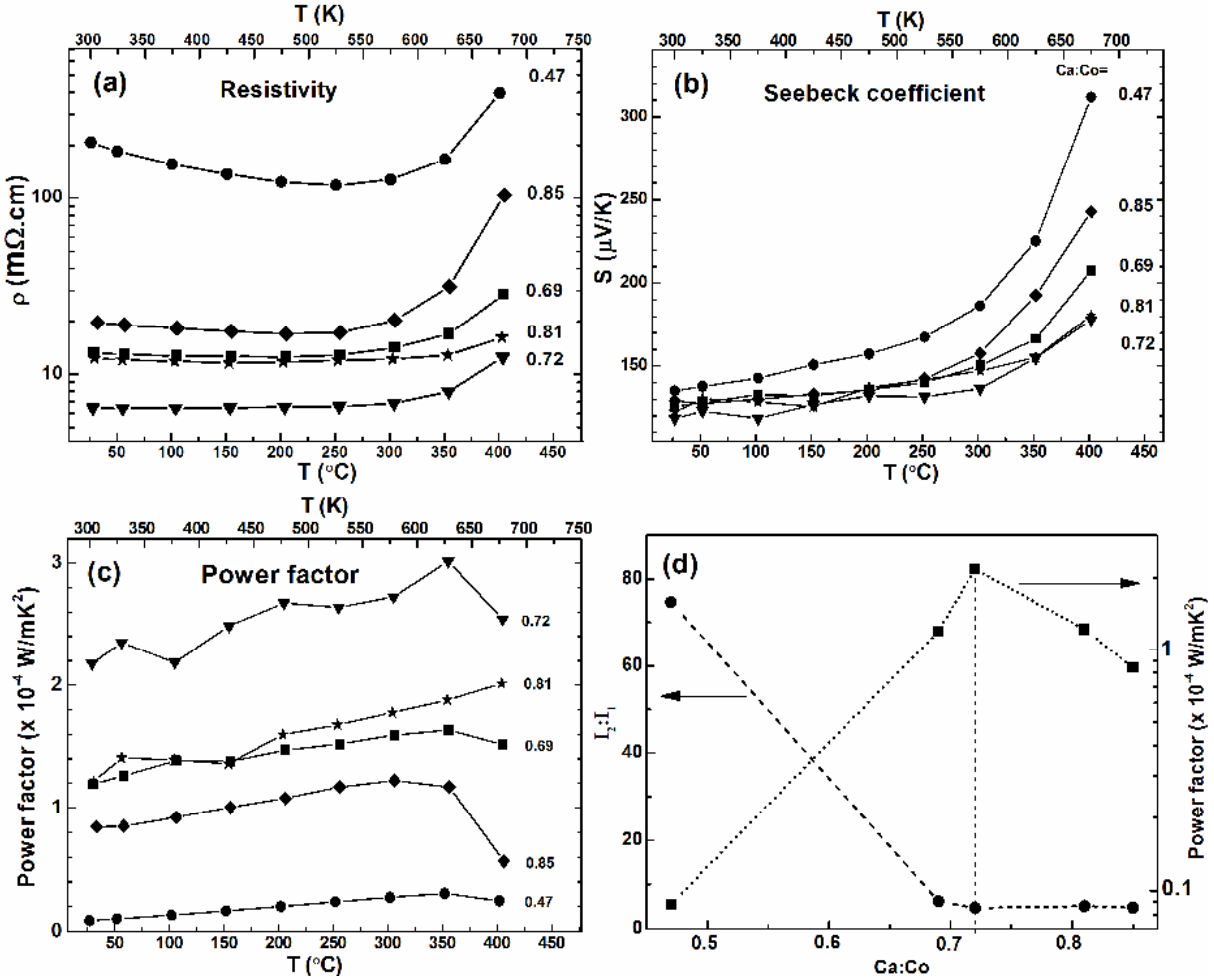

Figure 7. Temperature dependent a) electrical resistivity, b) Seebeck coefficient, and c) power factor for all samples as a function of elemental ratio Ca:Co. d) I_2/I_1 ratio and room temperature value of power factor as a function of elemental ratio Ca:Co.

DOI: 10.1002/ ((please add manuscript number))

Supporting Information

Mechanism of Formation of the Thermoelectric Layered Cobaltate $Ca_3Co_4O_9$ by Annealing of CaO-CoO Thin Films

Biplab Paul[*], *Jeremy L. Schroeder, Sit Kerdsongpanya, Ngo Van Nong, Norbert Schell, Daniel Ostach, Jun Lu, Jens Birch, Per Eklund*[*]

[1]Thin Film Physics Division, Department of Physics, Chemistry, and Biology (IFM), Linköping University, SE-581 83 Linköping, Sweden

[2]Dept. of Energy Conversion and Storage, Technical University of Denmark, Risø Campus, Frederiksborgvej 399, Building 779, 4000 Roskilde, Denmark

[3]Helmholtz-Zentrum Geesthacht, Centre for Materials and Coastal Research, Institute for Materials Research, Max-Planck-Straße 1, 21502 Geesthacht, Germany

Keywords: Thermoelectrics, $Ca_3Co_4O_9$, thin film, sputtering, phase transformation

*Corresponding authors. E-mail bippa@ifm.liu.se; perek@ifm.liu.se

Pole figure X-ray diffraction analysis

Pole figure x-ray diffraction analyses of the annealed film with Ca:Co=0.72 were performed. The (006) and (104) planes for the sapphire substrate and (002) and (203) planes for $Ca_3Co_4O_9$ were scanned. For the (006) and (104) planes of sapphire, 2θ angles of 41.67° and 35.13°, respectively, were set, whereas for the (002) and (203) planes of $Ca_3Co_4O_9$, the corresponding 2θ angles were 16.50° and 48.63°, respectively. All scans were performed with a tilt-angle (ψ) range 0 – 85° (step size 5°) and azimuth-angle (ϕ) range 0 – 360° (step size 0.1°).

The 006 pole figure of the sapphire substrate in Figure S1a and the 002 pole figure of the $Ca_3Co_4O_9$ film in Figure S1b show that both the film and substrate have the same out-of-plane orientation, i.e., the epitaxial relation between the film and the substrate in out-of-plane direction is $\{001\}Ca_3Co_4O_9 \| \{001\}Al_2O_3$. The three peaks in the pole figure in Figure S1c correspond to the {104} planes of the trigonal structure of sapphire. The six peaks in Figure S1d correspond to the {203} planes of monoclinic structure of $Ca_3Co_4O_9$. Because of the monoclinic structure of $Ca_3Co_4O_9$, there should be one peak in the pole figure pattern from the (203) plane. The reason for why six peaks are observed is that there are six twinned domains of $Ca_3Co_4O_9$ related to the trigonal symmetry of the substrate rotated at 60° from each other.[1] This is consistent with the reduced mismatch of the parameters of the substrate (4.76 Å) and the cobaltate (4.84 Å) and between $a\sqrt{3}$ of the substrate (8.24 Å) and $3 \times b_2$ (3 × 2.82 Å) of the CoO_2 cobaltate subsystem. Thus, the in-plane epitaxial relation between the film and the substrate is $\langle 010 \rangle Ca_3Co_4O_9 \| \langle \bar{2}10 \rangle Al_2O_3$.

[1] R. Moubah, S. Colis, C. Ulhaq-Bouillet, G. Schmerber, N. Viart, M. Drillon, A. Dinia, D. Muller, J. J. Grob *Eur. Phys. J. B* **2008**, 66, 315.

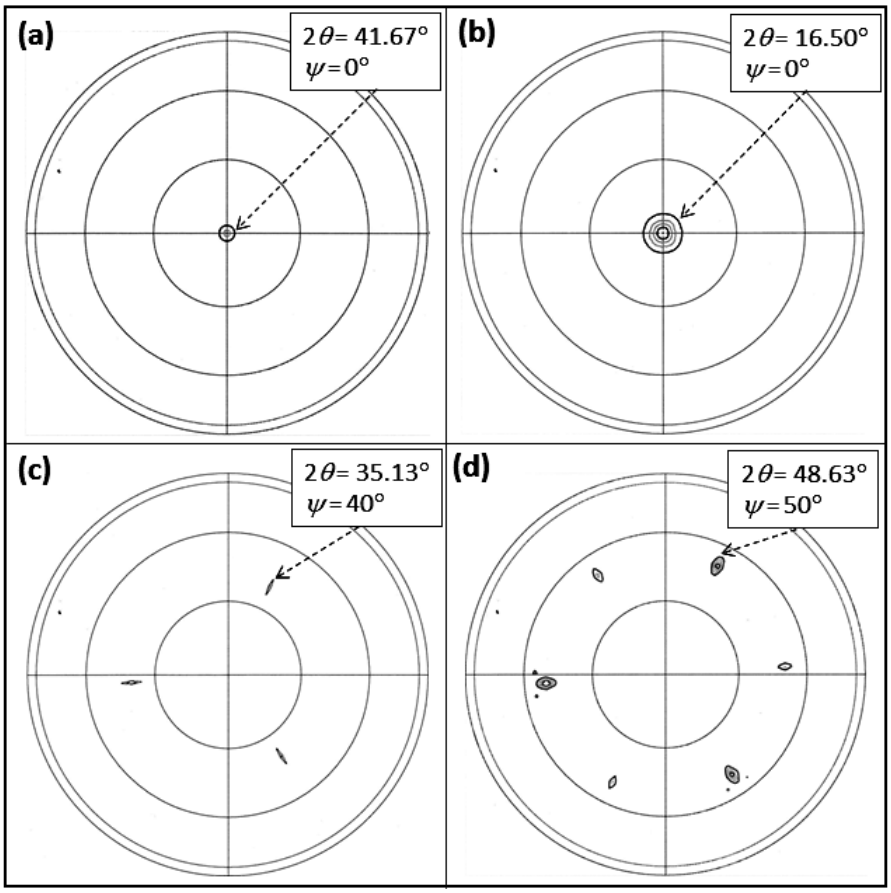

Figure S1. X-ray diffraction pole figures: a) (006) plane of the sapphire substrate; b) (002) plane of $Ca_3Co_4O_9$ film; c) (104) plane of the sapphire substrate; d) (203) plane of $Ca_3Co_4O_9$ film.

Additional transmission electron microscopy

A representative TEM image of an as-deposited film with Ca:Co=0.72 is shown in Figure S2. Energy dispersive spectroscopy (EDS) mapping shows Ca-deficiency near the interface. Such irregular distribution of Ca is attributed to the thermally induced diffusion of Ca from interface region towards the film surface due to the substrate heating during film deposition.

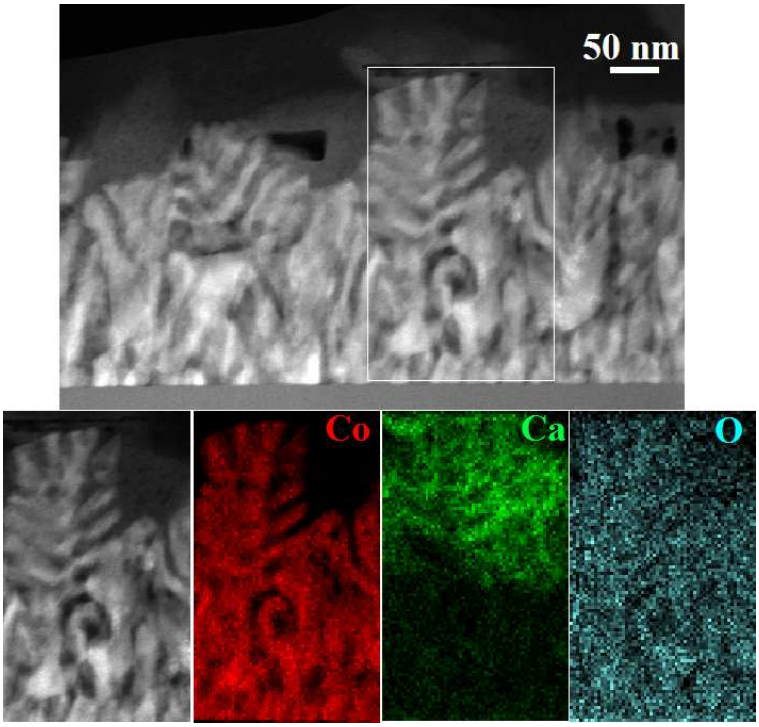

Figure S2. (top) Typical TEM image of as deposited CaO-CoO film and (bottom) EDS mapping of the selected area marked in the TEM image.

The substrate roughness can affect the quality of $Ca_3Co_4O_9$ film, which is evident from the presence of grains with different out of plane orientation in the film (see Figure S3a). A step of ~2 nm on the substrate surface (see Figure S3b) may be the cause the formation of this grain. The layers of the grain are parallel to the step side, which is comprised of Ca_xCoO_2 near the step side but of $Ca_3Co_4O_9$ in the region about 5 nm away from step side.

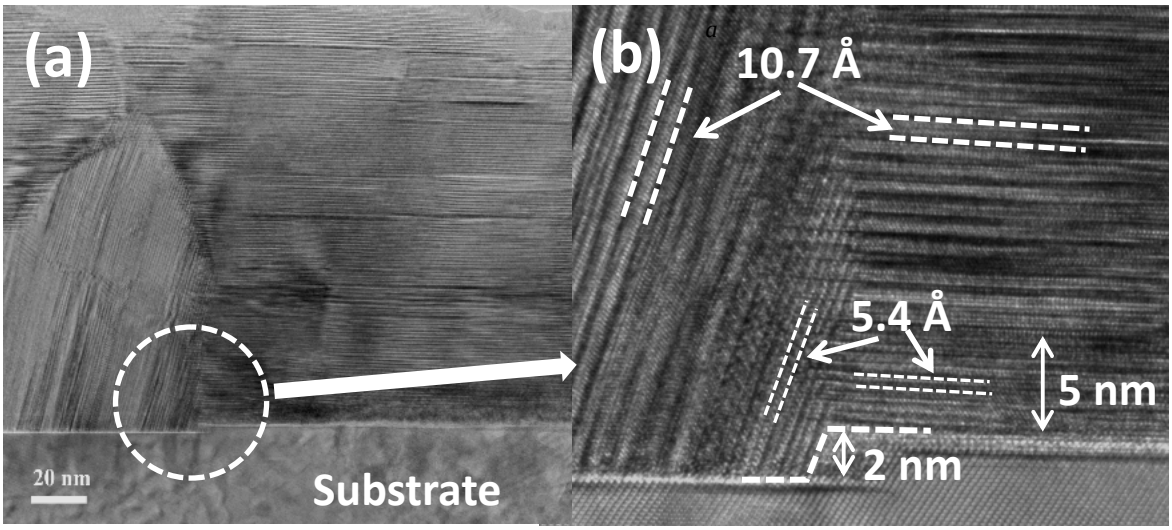

Figure S3. a) A typical TEM image of Ca:Co=0.72 annealed film shows the presence of tilted grain in the film is induced by the step on substrate surface. b) Magnified TEM image showing 2 nm step on the substrate surface.

TABLE OF CONTENTS ENTRY

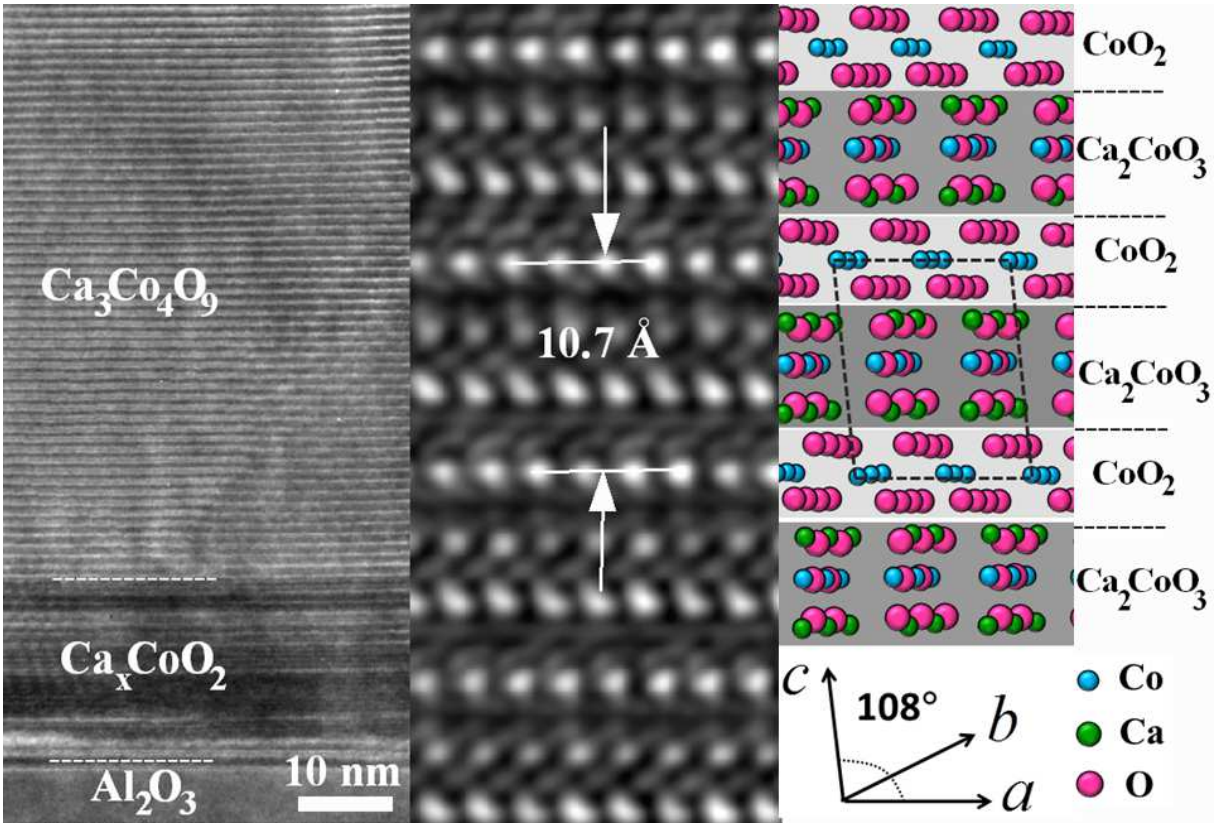

This study shows a novel two step sputtering/annealing method for thin film growth of highly textured $Ca_3Co_4O_9$. CaO-CoO thin film was deposited by reactive rf-magnetron co-sputtering from Ca and Co targets. Synchrotron-based 2D x-ray diffraction as well as ex-situ annealing experiments and standard lab-based x-ray diffraction analyses reveal the underlying mechanism of thermally activated phase transformation from CaO-CoO phase to the final phase of $Ca_3Co_4O_9$.